The Dependence of the Measured Surface Energy of Graphene on Nanosheet Size

Auren Ferguson, Andrew Harvey, Ian J Godwin, Shane D Bergin* and Jonathan N Coleman*

School of Physics, CRANN and AMBER Research Centres, Trinity College Dublin, Ireland

berginsd@tcd.ie, colemaj@tcd.ie

ABSTRACT: The surface energy of graphene nanosheets is surprisingly poorly known, probably due to size effects and energetic heterogeneities. Here we use finite-dilution inverse gas chromatography to measure the surface energy of liquid-exfoliated, few-layer graphene nanosheets of different sizes as a function of probe coverage. In all cases, the surface energy falls with probe coverage from a defect-controlled, low-coverage value to a value that approaches the basal plane surface energy at high coverage. We find an intrinsic basal plane dispersive surface energy of 61 ± 4 mJ/m^2, close to the value of 63 mJ/m^2 found for graphite. By comparison with similar data measured on graphite and using simple models, we can use the length dependence of the low coverage surface energy to differentiate between the effects of edge and basal plane defects, finding these to contribute ~130 and 180 mJ/m^2 to the surface energy respectively. From this data, we estimate a basal plane defect content of ~6×10^{14} defects/m^2 for both graphite and graphene in reasonable agreement with Raman data. This work shows that, in terms of surface energetics, few-layer graphene nanosheets behave exactly like graphite with the only differences associated with platelet dimensions.

INTRODUCTION

Graphene is one of the most exciting materials currently under active investigation. Due to its combination of unprecedented intrinsic properties and unrivalled applications potential, graphene research has made a significant impact in the fields of physics, chemistry, materials science and biology.(1) One of the most exciting things about graphene monolayers is that they are all surface. Even few-layer graphene nanosheets have relatively high surface to volume ratios. This makes graphene's ability to participate in surface and interfacial interactions a topic of great practical interest.

The simplest types of interaction to occur at graphitic surfaces are van der Waals interactions (dispersive interactions as well as specific interactions such as dipole-induced dipole etc).(2)

Such interactions can occur between graphene and neighbouring molecules(3, 4) or between adjacent graphene sheets for example.(5) The simplest way to describe such interactions us to express molecule-graphene or graphene-graphene binding energies in terms of the surface energy of graphene. Because of the non-polar nature of graphitic surfaces, the surface energy of graphene is expected to be dominated by the dispersive component. This is supported by the fact that even for polar 2-dimensional materials such as $Ni(OH)_2$, the contribution of specific interactions to the surface energy is quite small relative to the dispersive component.(6) This allows one to focus on the dispersive surface energy which can be expressed as an intrinsic property via the Fowkes relation(7) which gives the dispersive work of adhesion per unit area of surface A in contact with surface B as $W_{A-B} = 2\sqrt{\gamma_d^A \gamma_d^B}$, where γ_d^A and γ_d^B are the surface energies of surface A and B respectively. Expressing the dispersive surface energy of graphene as γ_d for simplicity, this means the areal work of adhesion for two graphene surfaces is $W_{Gra-Gra} = 2\gamma_d$ for example. Knowledge of γ_d is important in a range of areas, from estimating the binding energy of adsorbents to choosing solvents for graphene exfoliation (successful solvents are those with surface energy matching that of graphene).(8)

One might imagine that γ_d would be well known for a material like graphene or indeed its parent material, graphite. However, this is not the case. Even for graphite, a material that has been intensively studied for 70 years, a very wide range of values (see our previous work for a summary(9)) have been reported in the literature for its surface energy, from ~27-875 mJ/m^2. Even for graphene, the spread is worryingly broad with values reported in the range 35-115 mJ/m^2.(10-18) This may be partly due to contamination effects. It is well-known that graphitic surfaces very easily become contaminated with hydrocarbons which tend to alter the effective surface energy.(15) However, another important reason for this variation is surface heterogeneity: In the real world neither graphene nor graphite consist of only graphitic carbons but also contain defects which can have an impact on the surface energy. The effects of such defects can be magnified depending on how the surface energy is measured. For example, in infinite dilution inverse gas chromatography (see below), very small quantities of probe molecules are used to measure the surface energy. If defects bind the probe molecules more strongly than graphitic carbon atoms do, then the outputted surface energy will be dominated by the effects of defects.(14, 19) Conversely, contact angle measurements(14) probe the whole surface and as such give a weighted average of the contributions of defects and graphitic carbons, rather than an intrinsic surface energy associated with the basal plane. We would

expect defects to come in a number of types including basal plane defects and edge defects.(9, 14) Because the edge population depends on nanosheet size,(9) one would expect the defect contribution and so the surface energy as a whole to be strongly nanosheet-size-dependent. Thus, the spread in measured surface energies is hardly surprising. What is required is a method to differentiate the effects of edge and basal plane defects from the basal plane surface energy. Such a method would allow us to isolate intrinsic from extrinsic effects and gain a clearer insight into surface and interfacial interactions in graphene.

Recently, we reported such a method which we applied to the surface energy of graphite.(9) This method involves using finite-dilution inverse gas chromatography (FD-IGC) to measure the surface energy as a function of probe coverage. This allows us to separate the effects of defects from those of basal plane graphitic carbons. Then, by comparing measurements on samples of different sizes, one can separate the effects of edge and basal plane defects. Here, we apply this technique to liquid exfoliated graphene. Our results demonstrate that few-layer graphene shows surface energy parameters which are identical to graphite with the individual results differentiated only by nanosheet dimensions.

INVERSE GAS CHROMATOGRAPHY THEORY

IGC is surface characterisation technique used in a number of fields including pharmacy,(20) polymer chemistry(21) and mining.(22) Whilst techniques such as contact angle require a smooth flat surface to measure surface energy, IGC holds the advantage in that it can be used on particulates, flakes, powders or films. Although IGC is usually used for measuring surface energy of solids,(23) it also has other applications such as measuring surface area,(24) solubility parameters(25) and glass transition temperatures in polymers.(26)

In IGC, known probe solvents such as n-alkanes are injected into a column packed with the sample to be examined. The amount of solvent transmitted through the column is then recorded as a function of time in the form of a chromatogram with the adsorption-desorption behaviour of the probe on the solid surface inferred from the retention time, t_r. This is the time taken for the probe to elute through the column and can be used to calculate the net retention volume, V_N which is a fundamental thermodynamic property of solid-vapour interactions, using the equation:

$$V_N = \frac{j}{m} F(t_r - t_0) \left(\frac{T}{273.15 \text{ K}} \right) \tag{1}$$

Here j is the James-Martin correction factor,(27) m is mass of sample in the column, F is the carrier gas flow rate, t_0 is the dead time (time taken for non-interacting probe to elute through the column) and T is the column temperature. Once V_N has been measured, it can be used to calculate a range of parameters, most commonly the surface energy.

For a van der Waals bonded material, the surface energy, γ, is the sum of the dispersive surface energy, (γ_d) and specific surface energy (γ_s) (24). The dispersive surface energy of a material has its basis in London (or dispersion) interactions(28) while γ_s is associated with specific interactions between probe and solvent (*e.g.* dipole interactions or hydrogen bonding).(29) In this work we focused on γ_d measurements since the measured values are probe-solvent independent while values obtained for γ_s depend on the specific solvents used.(30) In addition, as indicated above, one would expect the dispersive component to dominate the surface energy of graphite. The Dorris-Gray method was applied in this case(31) which involves using a series of n-alkanes as probes to measure the free energy of adsorption, ΔG_{probe}. The dispersive free energy of one methylene group (ΔG_{CH_2}) can be calculated from slope of the graph of ΔG_{probe} *versus* the carbon number, n of the alkane probe using:

$$\Delta G_{CH_2} = -RT \ln\left(\frac{V_{N,n+1}}{V_{N,n}}\right) \tag{2}$$

where T is the column temperature and V_N is the net retention volume calculated by equation 1. ΔG_{CH_2} is related to the work of adhesion, W_{CH_2} by:

$$\Delta G_{CH_2} = -N_a a_{CH_2} W_{CH_2} \tag{3}$$

where N_a is Avogadro's number and a_{CH_2} is the surface area of a methylene group. For non-polar probes W_{CH_2} is found *via* the Fowkes relation:(7)

$$W_{CH_2} = 2\sqrt{\gamma_d \gamma_d^{CH_2}} \tag{4}$$

where $\gamma_d^{CH_2}$ is the dispersive surface energy of a methylene group which is calculated by $\gamma_d^{CH_2} = 35.6 + 0.058(293 - T)$.(32) By combining equations 2, 3, 4 and rearranging we get an expression for γ_d, the dispersive surface energy of the solid sample:

$$\gamma_d = \frac{1}{4\gamma_d^{CH_2}} \left[\frac{RT \ln\left(V_{N,n+1}/V_{N,n}\right)}{N_a a_{CH_2}} \right]^2 \tag{5}$$

where $RT \ln\left(V_{N,n+1}/V_{N,n}\right)$ is the slope of alkane line from the plot $RT \ln V_N$ versus carbon number of the alkane probe.

The experiments described here were performed using a Surface Energy Analyser (SEA) which is the latest generation of IGC apparatus and makes measuring the surface energy of energetically heterogeneous materials more reliable via the ability to control the specific surface coverage of probe molecule. At low probe concentrations, the surface coverage is very low and so only probe-sample interactions occur. Then only surface sites with high probe-surface binding energy are investigated. This is the standard form of IGC and is called infinite-dilution IGC (ID-IGC).(32)

The advantage of the SEA is that it can accurately control the coverage of probe molecules on the surface. This is achieved by the controlling probe injection time which relates to the surface coverage. One must consider both the actual and targeted surface coverage, where the target is related to the ideal injection time (based on the specific surface area of the sample) and the actual is associated with the measured injected quantity. In the experiments carried out here, the difference between target and actual surface coverage is no more than 10%. This allows the SEA to measure so-called surface energy profiles, *i.e.* the surface energy as a function of probe coverage. This is termed finite-dilution IGC (FD-IGC),(33) and is important because it facilitates the characterisation of not just high energy sites but also sites with lower probe-surface binding energy. Such sites become important only as the probe coverage is increased. Thus, a typical surface energy profile shows a high surface energy value at low coverage due to the presence of high energy sites. However, at the coverage increases, the surface energy drops off, as the probe molecules begin to access the low energy sites.

In practise, the retention volume is measured for a set of alkane probes at a given coverage and the surface energy calculated using equation 5. This procedure is repeated at a range of coverages to produce a surface energy profile. In all cases, the specific surface area (S_{BET}) of a sample must be known to accurately relate injection volumes to surface coverage. The specific surface area measurement is described in the supplemental information. While the Dorris-Gray method was initially developed for infinite dilution systems(34), it has become standard practise to extend the Dorris-Gray method to finite dilution systems like the ones in

this work.(22, 35-37) However, it must be noted that at higher coverages, the assumptions underpinning the Dorris-Gray method may not hold and so high-coverage results must be treated with caution.

RESULTS AND DISCUSSION

Basic characterisation

We produced graphene nanosheet dispersions by liquid phase exfoliation(8) of graphite (Timcal) in the solvent N-methyl-pyrrolidone using high shear mixing(38) (see methods). Such dispersions contain largely defect-free nanosheets with lateral sizes (defined here as the length, *L*, of the longest dimension) between ~50 nm and ~5 μm and thicknesses (usually expressed as number of monolayers per nanosheet, *N*) between 1 and ~15 layers. We used liquid cascade centrifugation(39) to separate the as-prepared dispersion into six fractions with different sizes and thicknesses. These fractions were labelled XS, S, M, XL, XL and XXL in ascending order of nanosheet size. Shown in figure 1A-B are example TEM images of nanosheets taken from the XS and XXL batches respectively. The size difference between these fractions is clear. The lateral nanosheet size (*i.e*. *L*) in each fraction was quantified by statistical analysis of the TEM images with histograms for the largest and smallest fractions shown in figure 1C. As observed previously, the size distributions are very close to lognormal distributions.(39, 40) The mean nanosheet length in each fraction varied from 400 nm (XS) to 2.2 μm (XXL).

For the IGC measurement, the solvent was removed by vacuum filtration to give a reaggregated powder. This powder was first analysed using Raman spectroscopy. Example spectra are shown in figure 1D for the largest and smallest fraction with each displaying the characteristic D, G and 2D bands.(41) The 2D band is particularly interesting as it is very sensitive to the nanosheet thickness. Previously, we proposed a quantitative metric (labelled M_2 in Backes *et al.*(40)) which allows the mean nanosheet thickness in the dispersion to be extracted from the shape of the 2D band. We have applied this metric, finding mean nanosheet thicknesses ranging from 6.6±1 monolayers for the XS sample to 10±2 layers for the XXL sample. We note that as the nanosheet thickness increased from sample XS to XXL, the 2D band shape shifted closer and closer to that of the starting graphite (see SI). However, it never reached the graphitic lineshape showing that even the thickest nanosheet sample retained graphene-like properties. We have plotted the mean nanosheet thickness versus the mean length (extracted from TEM) in figure 1E. This graph clearly shows the nanosheet length to vary much

more significantly over the fractions than the thickness. This makes these samples well suited to studying the effects of length on the nanosheet surface energy.

The Raman D-band (~1360 cm^{-1}) is known to scale with the defect content.(40, 42, 43) For graphene nanosheets, it has been shown that the ratio of D-band to G-band (~1580 cm^{-1}) intensities, I_D/I_G, scales linearly with $1/L$ due to the presence of nanosheet edges which act as defects.(40) This can be expressed as

$$I_D / I_G \approx (I_D / I_G)_{Basal} + \kappa / \langle L \rangle, \tag{6}$$

where $(I_D / I_G)_{Basal}$ is the contribution to I_D/I_G from basal plane defects and κ is a parameter which depends on the Raman scattering process, properties of the graphene itself and the nanosheet shape distribution.(40) This behaviour is shown in figure 1F for the nanosheets prepared here with the datum close to $1/L=0$ representing the unexfoliated graphite. This graph suggests the basal plane defect content of the graphene to be similar to that of the graphite and shows the length-dependence of the defect content to be due to changes in the edge population.

In order to facilitate the surface energy measurements and to learn more about the state of the material, we measured the specific surface area of these reaggregated powders (see methods and SI). Shown in figure 1G is a graph of the specific surface area as a function of mean nanosheet length. This graph clearly shows a significant length-dependence with values ranging from ~65 to ~40 m^2/g. Though these value appear low, this is almost certainly due to aggregation effects during drying (see below). We can model this by noting that the nanosheets in the reaggregated powder have two contributions to their surface area – the basal plane and the edge – such that:

$$S_A = \frac{2A + Pt}{\rho A t} \tag{7a}$$

where A is the basal plane area, P is the nanosheet perimeter length and t is the nanosheet thickness. As shown in our recent work,(9) the ratio of perimeter length to nanosheet area can be approximated in terms of L and the nanosheet length/width aspect ratio, k: $P / A = 4\sqrt{1+k^2} / L$. In addition, we note that reaggregation effects will mean that the nanosheets in the reaggregated sample may be significantly thicker than those in the dispersion. (We note that, as shown by their Raman response,(40) these aggregated nanosheets generally consist of randomly stacked arrays of few-layer nanosheets, rather than Bernal-stacked monoliths, and so should not be considered to be graphite.) This allows us to write the

reaggregated nanosheet thickness as $t = R_N d_0 N$, where d_0=0.35 nm is the monolayer thickness and $R_N = N_{agg} / N$ is the ratio of the mean number of stacked monolayers in an aggregated nanosheet, N_{agg}, to the mean number of monolayers in a few-layer nanosheet in the dispersed state (N). Combining these factors and rearranging gives:

$$S_A L = \frac{2}{\rho R_N d_0} \frac{L}{N} + \frac{4\sqrt{1+k^2}}{\rho}$$ (7b)

To test this, we have plotted $S_A L$ versus L/N in figure 1H, finding good linearity. This supports our simple model and shows that the ratio $R_N = N_{agg} / N$ is constant over all fractions. Fitting the data with equation 7b gives k=1.87±0.8 and R_N=7.6±0.6. This value of k is very close to the value of k=1.75 found from statistical analysis of the TEM images. In addition, the value of R_N is consistent with recent data on WS_2 nanosheet supercapacitors which suggests the aggregated nanosheet thickness in filtered films to be approximately five times that in the liquid dispersion.(44)

Finite-dilution inverse gas chromatography measurements

In order to ascertain how the surface energy of different size-selected graphene samples differ from each other, their dispersive surface energy (γ_d) profiles were measured using coverage-dependent IGC. These measurements were performed on reaggregated powders with SEM images of samples containing the smallest and largest nanosheets shown in figure 2A-B. Surface energy profiles are measured by injecting a series of n-alkane probes from hexane to octane at selected surface coverages. Surface coverage (ϕ) is calculated as a fraction of the monolayer capacity of the sample from specific surface area measurements (figure 1G). Shown in figure 2C are two alkane plots, portraying the Gibbs free energy of adsorption (ΔG_{probe}) as a function of alkane carbon number, n, measured at low and high probe coverage (from XL graphene). At any coverage γ_d is calculated using the slope of the alkane plot and Doris-Gray formula as shown in equation 5. This process is repeated for all coverages to complete the γ_d profile. Due to injection limitations of the SEA, 3 alkane probes were used to measure γ_d. Generally, in the literature, at least 4 alkane probes are used to measure γ_d. However, there are also many examples where only 3 alkanes are used.(36, 45-47)

Figure 2D shows the γ_d profiles of two of the graphene samples used in this study (the rest are shown in the SI). The profiles have the usual concave shape, with surface energy falling with increasing probe coverage(48) from the low-ϕ value of $\gamma_{d,\phi=0}$, to the full coverage surface energy $\gamma_{d,\phi=1}$. Significant variations in surface energy profiles were observed from sample to sample. It is worth noting that some of these coverage curves are slightly different to those usually found, in that the surface energy does not saturate at high coverage (e.g. XS). As will become clear below, this is due to the large defect content associated with these small, edge-rich nanosheets.

For the size selected graphene studied here, we observed values of $\gamma_{d,\phi=0}$ in the range 124-144 mJ/m^2 while $\gamma_{d,\phi=1}$ values were in the range 57-69 mJ/m^2 (figure 2E). To the best of our knowledge, there has been no reported IGC surface energy measurements done on pristine graphene. However, there have been ID-IGC studies on reduced graphene oxide (RGO) that show reasonable agreement with the measured values of $\gamma_{d,\phi=0}$ here. Dai *et al* have produced two studies on the low-coverage γ_d of RGO and values that range from 89-106 mJ/m^2 measured using ID-IGC.(10, 11)

However, the full coverage values ($\gamma_{d,\phi=1}$) measured here (57-69 mJ/m^2) are far lower than the literature ID-IGC values quoted above and are more comparable to values of surface energy measured by contact angle (49) or suggested by solubility measurements(8) which tend to fall in the range 35-85 mJ/m^2.(12-18, 49) This is consistent with the fact that $\gamma_{d,\phi=1}$ reflects the adsorption of molecules onto the whole surface and not just the highest energy sites. In addition, it matches well to graphene surface energy values predicted by liquid phase exfoliation measurements which are consistent with a graphene surface energy of ~70 mJ/m^2.(8, 50)

Although, it is possible to use a two-state model to derive an equation for the coverage dependence of the adsorption enthalpy,(19) most papers use a less rigorous approach. In the literature, γ_d profiles for energetically heterogeneous surfaces are often empirically fitted to an exponential decay function,(36, 51) which has been written as:(9)

$$\gamma_d(\phi) = \gamma_{d,\phi=1} + (\gamma_{d,\phi=0} - \gamma_{d,\phi=1})e^{-\phi/\phi_0} \qquad (8a)$$

where $\gamma_{d,\phi=1}$ is the dispersive surface energy at full coverage, $\gamma_{d,\phi=0}$ is the dispersive surface energy at zero coverage, and ϕ_0 is a constant which describes how fast the surface energy decays with increasing coverage. We note that this notation is slightly inappropriate here due to the fact that the surface energy profiles do not saturate at high coverage. Thus, when fitting to our data, $\gamma_{d,\phi=1}$ actually represents the surface energy when the coverage is projected to values well beyond one. However, for convenience, we will retain the nomenclature given above. Recently, we showed that a stretched/compressed exponential tends to match the data much better and give more consistent results:(9)

$$\gamma_d(\phi) = \gamma_{d,\phi=1} + (\gamma_{d,\phi=0} - \gamma_{d,\phi=1})e^{-(\phi/\phi_0)^K} \quad\quad\quad (8b)$$

where K is the stretching (when $0<K<1$) or compression ($K>1$) exponent. We have fitted all coverage-dependent surface energy data to equation 8b, extracting $\gamma_{d,\phi=1}$, $\gamma_{d,\phi=0}$, ϕ_0 and K. As shown in figure 2D good fits were obtained with values of K between 0.8 and 1.1 (see SI for all fits).

However, some caution is required here. While equation 8a is widely used in the literature and figure 8b has been shown to fit surface energy profiles of graphite very well, we have observed some deviations from smooth exponential-like decay (see SI). Such deviations are likely to be secondary effects and indicate the presence of more complex behaviour beyond the simple picture outlined here. For example, our data may contain larger-than-usually-observed effects associated with probe-probe interactions. Such effects may be particularly important for samples such as those measured here, because the high proportion of edge defects found in small nanosheets requires us to collect data out to large coverages, increasing the potential impact of probe-probe interactions. Thus, while we believe the methodology used here is valid, we would advise that care be taken when measuring samples with high defect contents.

Shown in figure 2E is a plot of $\gamma_{d,\phi=1}$ *versus* $\gamma_{d,\phi=0}$, showing no simple correlation between these parameters suggesting that they may be independent of each other, as found recently for graphite.(9) This implies that high energy sites (probed at low coverage) on the sample surface are not representative of the surface as a whole (probed at high coverage) and so carry little information about the intrinsic surface properties. This shows the importance of coverage dependent IGC compared to ID-IGC. We have plotted both $\gamma_{d,\phi=1}$ and $\gamma_{d,\phi=0}$ (both

extracted from the fits to equation 8b) versus ϕ_0 in figure 2F. Here, $\gamma_{d,\phi=1}$ appears to be independent of ϕ_0 with a value close to 60 mJ/m². This is very similar to the result found recently for graphite. The value of $\gamma_{d,\phi=0}$ decays weakly with ϕ_0, falling from 140 to 120 mJ/m². However, for graphite the magnitude of the decay was much larger: as ϕ_0 increased, $\gamma_{d,\phi=0}$ fell smoothly from ~175 to ~120 mJ/m² in the range $0.04 < \phi_0 < 0.24$. The reasons for these differences will be discussed below.

In line with previous work on the surface energy of graphite by Otyepka et al(19, 52) as well a recent paper from our group,(9) we believe the high-energy sites probed at low-coverage are associated with defects in the graphene lattice. These can either be associated with the flake edges or basal plane defects such as point defects (e.g. Stone-Wales defects, vacancies or double vacancies(52)). Conversely, the dominant low-energy sites probed at high-coverage represent the basal plane in the absence of defects.(9, 19) If this model is correct, $\gamma_{d,\phi=1}$ can be associated with the intrinsic surface energy of graphene in the absence of defects or edges and should be independent of flake dimensions. Conversely we would expect $\gamma_{d,\phi=0}$ to display some size dependence associated with the relative edge/basal plane defect populations. For very large graphitic platelets, the edges are negligible meaning we would expect $\gamma_{d,\phi=0}$ to be dominated by the effects of basal pane defects. Conversely, for very small nanosheets, the resultant population of edge sites will have a significant impact on $\gamma_{d,\phi=0}$. Both of these predictions have been verified for graphite nanoplatelets.(9)

To test these ideas for graphene nanosheets, we plot both $\gamma_{d,\phi=0}$ and $\gamma_{d,\phi=1}$ versus nanosheet length in figure 3 A-B. We do indeed find $\gamma_{d,\phi=1}$ to be independent of nanosheet length as expected with a mean of 61±4 mJ/m². Thus, we can associate $\left\langle \gamma_{d,\phi=1} \right\rangle = 61 \pm 4$ mJ/m² with the intrinsic surface energy of graphene in the absence of defects or edges. This is similar to the measured mean dispersive surface energy of commercial graphite, which was found(9) to be $\left\langle \gamma_{d,\phi=1} \right\rangle = 63 \pm 7$ mJ/m². However, this may not be exactly correct as the graphene used in this study was not exceptionally clean and would have been initially contaminated by residual solvent. The annealing process applied was not particularly aggressive and was unlikely to result in a truly pristine graphitic surface. This means the values of $\gamma_{d,\phi=1}$ obtained may not

correlate exactly with the true surface energy of graphene but more accurately reflect the surface energy of a graphitic surface contaminated with hydrocarbons.(15)

We now turn to the $\gamma_{d,\phi=0}$ data which appears to display a weak length dependence, increasing from ~125-140 mJ/m². On the face of it, this is consistent with our previous work on the surface energy of graphite which showed a steady increase in $\gamma_{d,\phi=0}$ from values of ~130 mJ/m² for small graphite platelets with L~15 μm to $\gamma_{d,\phi=0}$~180 mJ/m² for much larger platelets with lateral dimensions approaching 1 mm.(9) We interpreted this graphite data using insights garnered from computational studies(9) as follows. Computational studies showed $\gamma_{d,\phi=0}$ to depend strongly on the position of the deepest sites in the surface energy distribution. As indicated above, the overall surface energy distribution has three components: normal basal plane carbons, basal plane defects and edge defects. Because both types of defect sites tend to be deeper (contribute higher surface energy values) than basal plane sites, they dominate the measured value of $\gamma_{d,\phi=0}$. When the graphite platelets are very large, there are very few edges and $\gamma_{d,\phi=0}$ is predominately due to basal plane defects. In this case, the measured value of $\gamma_{d,\phi=0}$ ~180 mJ/m² indicates such basal plane defects to be relatively deep. On the other hand, when the graphite platelets are very small, there are many more edge defects compared to basal plane defects and so edges dominate $\gamma_{d,\phi=0}$. Again, because the small-platelet value of $\gamma_{d,\phi=0}$ measured for graphite is ~130 mJ/m², considerably smaller than the large-flake limit, we suggest the edge defect binding sites to be energetically shallower than basal plane defect sites (although deeper than the regular basal plane sites which tends to contribute ~60 mJ/m² to the surface energy). We believe this interpretation also applies to the graphene data presented here. However, care must be taken here as calculations have suggested that, for acetone adsorption, edge defects have a higher binding energy that basal plane defects,(52) the opposite to that suggested by our results for alkanes. This highlights the fact that the details of absorption energetics might vary considerably, especially for polar molecules.

The decay constant, ϕ_0, is a measure of the coverage required to fill most of the high energy sites such that the probe molecules start to interact with the low energy sites. This implies that ϕ_0 is proportional to the fraction of defect sites. This hypothesis is easily tested by plotting ϕ_0 versus I_D/I_G, which is known to scaling with the defect density in graphene.(40, 43) This data is shown in figure 3C and shows the expected linear scaling. This means that we would expect to see a reduction in ϕ_0 as the graphene nanosheet size is increased and so the

population of edge defects decreases.(9) This is exactly what is observed (figure 3D), indicating that the graphene surface energy data is qualitatively in line with previous measurements on graphite.

Quantitative analysis and comparison to graphite

After considerable preliminary analysis, we realised that the most revealing way to quantitatively analyse the graphene data was alongside the graphite data from our previous work.(9) To this end, in figure 4 we have plotted a number of relevant graphs involving $\gamma_{d,\phi=0}$, $\gamma_{d,\phi=1}$ and ϕ_0 data for both graphene (reported here, filled symbols) and graphite (originally reported in ref (9), open symbols). The simplest, and possibly most revealing graph, is a plot of both $\gamma_{d,\phi=0}$ and $\gamma_{d,\phi=1}$ versus ϕ_0 for both graphene and graphite which is given in figure 4A. It is clear from this graph that the graphene and graphite data sit on the same trend lines with $\gamma_{d,\phi=1}$ remaining constant while $\gamma_{d,\phi=0}$ decays steadily with ϕ_0.

The $\gamma_{d,\phi=1}$ data is clearly in line with the model described above linking it with the basal plane surface energy of graphene/graphite which we would expect to be size independent. To fully understand the $\gamma_{d,\phi=0}$ *versus* ϕ_0 data, a more quantitative approach is necessary. In our study of graphite we showed that ϕ_0 could be quantitatively modelled as proportional to the fraction of graphene surface area occupied by probe molecules when all defects have been saturated with probe molecules. We must consider a combination of both edge and basal plane defects. We assume that there are $N_{D,B}/A$ defects per unit area of basal plane and that around each defect is an area A_{HE} which acts as a high energy region for the absorption of probe molecules. We note that this area might be significantly larger than the actual defect size and represents the area where the carbon atoms have deviated from their defect-free positions. In addition, the whole of the edge region of a flake also behaves as an array of high energy sites for probe molecules. Then, by treating the flake as a platelet of area, A, perimeter length, P, and thickness, t, we can write:

$$\phi_0 = \beta \frac{A_{HE}(N_{D,B}/A)2A + Pt}{2A + Pt} \tag{9a}$$

where β is a proportionality constant linking ϕ_0 to the fraction of surface area associated with defects.(9) Again, using $P/A = 4\sqrt{1+k^2}/L$, this equation becomes:

$$\phi_0 = \beta \frac{A_{HE}(N_{D,B}/A) + 2\sqrt{1+k^2}\,t/L}{1 + 2\sqrt{1+k^2}\,t/L} \tag{9b}$$

In addition, by combining empirical observations from computational studies with physical arguments we showed[9] a semi-empirical relationship between $\gamma_{d,\phi=0}$ and platelet dimensions:

$$\gamma_{d,\phi=0} = \gamma_{d,\phi=0}(L=0) + [\gamma_{d,\phi=0}(L=\infty) - \gamma_{d,\phi=0}(L=0)]e^{-2\ln 2\sqrt{1+k^2}\left[A_{HE}(N_{D,B}/A)\right]^{-1}\times t/L} \tag{10a}$$

where

$$\Delta\gamma_{d,\phi=0} = \gamma_{d,\phi=0}(L=\infty) - \gamma_{d,\phi=0}(L=0) \tag{10b}$$

and $\gamma_{d,\phi=0}(L=0)$ and $\gamma_{d,\phi=0}(L=\infty)$ represent the mean surface energy contributions of edge defects and basal plane respectively.

Both of these equations require independent knowledge of t and L and so are limited by the quality of dimensional measurements available. However, this reliance on L and t can be avoided by combining these equations to eliminate t/L:

$$\gamma_{d,\phi=0} \approx \gamma_{d,\phi=0}(L=0) + 2\Delta\gamma_{d,\phi=0}\,e^{-\ln 2\times\phi_0\left[\beta A_{HE}(N_{D,B}/A)\right]^{-1}} \tag{11}$$

We note that these expressions allow us to extract four material parameters from the data: β, $A_{HE}(N_{D,B}/A)$, $\gamma_{d,\phi=0}(L=0)$ and $\gamma_{d,\phi=0}(L=\infty)$. The first two parameters are related to the defect content: knowledge of β allows the total areal fraction associated with high energy sites (defects) to be estimated from ϕ_0 while $A_{HE}(N_{D,B}/A)$ represents the fraction of basal plane surface area associated with basal plane defects.[9]

The solid green line in figure 4A is a fit to equation 11. It is clear that this line fits both graphene and graphite data equally well with $\gamma_{d,\phi=0}(L=0)=131\pm3$ mJ/m^2, $\gamma_{d,\phi=0}(L=\infty)=181\pm13$ mJ/m^2 and $\beta A_{HE}(N_{D,B}/A)=0.036\pm0.01$. While the values of $\gamma_{d,\phi=0}(L=0)$ and $\gamma_{d,\phi=0}(L=\infty)$ are close to those reported for graphite (125 and 180 mJ/m^2),[9] we believe the current values are more accurate due to the larger data set and better fit. Strictly speaking this data only shows that both graphene and graphite share the same product $\beta \times A_{HE}(N_{D,B}/A)$. However, we believe that both β and $A_{HE}(N_{D,B}/A)$ share the same values for graphene and graphite. Computational studies have indicated that β is a material parameter which depends on the details of the probe-surface binding site distribution $e.g.$ the centre points of the contributions

of edge defects, basal plane defects and basal plane graphitic carbons to the surface energy.(9) Thus, one would expect β to be the same for graphene and graphite. Turning to $A_{HE}(N_{D,B}/A)$, this parameter represents the fraction of basal plane surface area which contributes to the basal-plane defect binding site distribution. Clearly for $A_{HE}(N_{D,B}/A)$ to be different between graphene and graphite would require the areal defect density, $(N_{D,B}/A)$, to be different. However, if this were the case, for example if basal plane defects were created during exfoliation, one should see evidence in the Raman data. In particular, with reference to equation 6, basal-plane defect production during exfoliation would mean that $(I_D/I_G)_{Basal} > (I_D/I_G)_{Graphite}$ where $(I_D/I_G)_{Graphite}$ is the D/G ratio measured on the starting graphite. However, from the intercept in figure 1F, it is clear that $(I_D/I_G)_{Basal} \approx (I_D/I_G)_{Graphite}$ because the data point with 1/L~0 was measured on the starting graphite and this lies very close to the intercept of the fit. This implies the number of basal plane defects produced during exfoliation is very small and so $A_{HE}(N_{D,B}/A)$ has not changed measurably going from graphite to graphene. We note that this is as expected because here the graphene was produced by shear exfoliation which is a low-energy process and should not introduce defects.(38) Thus, we are reasonably confident that both β and $A_{HE}(N_{D,B}/A)$ share the same values for graphene and graphite.

We can now individually analyse the data for ϕ_0 and $\gamma_{d,\phi=0}$ as a function of t/L. For the graphene data, L was extracted from TEM as described above while t was found using $t = R_N d_0 N$. This value is appropriate as it represents the effective aggregated nanosheet thickness in the measured powder and so is most relevant when considering the area available to adsorbing molecules. Shown in figure 4B are data for ϕ_0 as a function of t/L plotted for both graphene and graphite (the thickness values for the graphite were extracted from the surface area data presented in ref(9)). We have fit the entire data set (graphene and graphite) to equation 9b, keeping the product $\beta A_{HE}(N_{D,B}/A)$=0.036±0.01 (solid line). This combined fit gives β=5±0.5 and $A_{HE}(N_{D,B}/A)$=(7.3±2.8)×10^{-3}.

We can also fit the $\gamma_{d,\phi=0}$ versus t/L data shown in figure 4C quantitatively using equation 10. Although this data is more scattered, probably due to errors associated with measuring t and L, we find a reasonable fit to both data sets with $\gamma_{d,\phi=0}(L=0)$=131±8 mJ/m^2, $\gamma_{d,\phi=0}(L=\infty)$

=181±13 mJ/m^2 and $A_{HE}(N_{D,B}/A)=(4\pm1)\times10^{-3}$. Taking $\beta A_{HE}(N_{D,B}/A)=0.036\pm0.01$ then gives β=9±5.

Finally, as we demonstrated previously, it is possible to combine equations 7a and 9a to eliminate t and by using $P/A=4\sqrt{1+k^2}/L$ to get

$$\left[\frac{\rho S_{BET}\phi_0 L}{4\sqrt{1+k^2}}\right]=\beta\times(N_{D,B}/A)A_{HE}\times\left[\frac{\rho S_{BET}L}{4\sqrt{1+k^2}}-1\right]+\beta \qquad (12)$$

Because all the square-bracketed parameters have been measured in this work, one can parameterise the data in accordance with equation 12 and plot a graph which gives linear behaviour. As shown in figure 4D we fit both data sets keeping $\beta A_{HE}(N_{D,B}/A)=0.036$, extracting a value of β=3.8±0.7 leading to $A_{HE}(N_{D,B}/A)=(10\pm5)\times10^{-3}$.

Fitting the data in figures 4B-D gives a spread of β and $A_{HE}(N_{D,B}/A)$ values in the range 3.8-9 and (4-10)×10^{-3} respectively. Averaging gives β=5.9±3 and $A_{HE}(N_{D,B}/A)=(7.1\pm3.8)\times10^{-3}$ where the error is the sum of the mean over the individual errors and the standard error of the mean. We note that these values are within error of the values reported previously for graphite but are expected to be more reliable.

It is known that basal plane defects such as adatoms distort the graphene lattice over a distance of ~2 nm from the centre of the defect.[53] This allows us to approximate $A_{HE}\sim12$ nm^2. From this, we can estimate $N_{D,B}/A\sim6\times10^{14}$ defects/m^2 of basal plane for both graphite and graphene. This is reasonably close to the value of ~10^{14} defects/m^2 estimated from the Raman spectrum of the starting graphite using Ferrari's method.[43] It is also in fair agreement with the population of neutral point defects measured for graphene by Barreiro et al (2.5×10^{15} defects/m^2).[9]

This work has shown that, in terms of their surface energetics, the graphene nanosheets studied here behave exactly like graphite platelets. The overall dataset is consistent with both materials having the same values of $\beta, A_{HE}(N_{D,B}/A)$, $\gamma_{d,\phi=0}(L=0)$ and $\gamma_{d,\phi=0}(L=\infty)$. However, we note that the sample containing the thinnest nanosheets had a mean layer number of N=6. Thus, it is important to state that we have not investigated thin graphene nanosheets or monolayers. Such structures may have surface energies which diverge from graphite. For example, very thin nanosheets may have reduced surface energy due to the reduction in non-

nearest neighbour interactions.(15, 54) While it would be interesting to perform FD-IGC on size-selected samples of very thin, graphene nanosheets,(39, 40) such measurements are technologically challenging from the analysis perspective due to the expected high values of ϕ_0. Future work will involve characterisation of the surface energy of such samples.

CONCLUSION

In conclusion we have measured the dispersive surface energy of liquid exfoliated graphene as a function of probe coverage for six different nanosheet sizes. By fitting the surface energy versus coverage curves, we can extract the surface energy associated with the basal plane as well as the defect contribution to the surface energy and information about the defect content. We have analysed all graphene surface energy data alongside previously published graphite data. By analysing the size dependence of the surface energy, we can differentiate between the contribution to the surface energy of edge and basal pane defects as well as estimating the basal plane defect density. We find that all data is consistent, with graphene and graphite platelets displaying the same surface energy behaviour, differentiated only by platelet dimensions.

EXPERIMENTAL METHODS

Timcal graphite was used as the starting graphite for exfoliation with N-Methyl-2-Pyrrolidone (NMP) (reagent plus 99%, Sigma Aldrich) being used as the solvent. Graphene was produced by shear exfoliation(38) of graphite using a L5M high shear laboratory mixer (32mm rotor diameter) from Silverson Machines Ltd, UK.

The procedure for the production of size selected liquid exfoliated graphene was as follows: 275g of graphite was mixed with 2.5L of newly opened NMP and this was shear mixed for 4 hours at 8000rpm. This was let to settle overnight (approximately 14 hours). After settling, the supernatant was removed and discarded, with fresh NMP (2.5L) being added and the shear process being repeated. This is called sediment recycling and has been shown to increase graphene yield.(8, 38, 55) The final shear exfoliation step was the same as above (8000rpm for 4 hours and settle overnight). Here, the supernatant was collected and put into 2 batches of 16, 50mL vials and were centrifuged at 300rpm for 2 hours using a Thermo Scientific Heraeus Megafuge. The supernatant from these were extracted and mixed together to get a stock solution. Part of the sediment from this was kept as the first size selected sample, called XXL. Further size selection of the graphene was done using a method called liquid cascade

centrifugation; a detailed description of this can be found in Backes et al.(39) Here, the stock solution was centrifuged at 500rpm (47g) for 2 hours and the sediment was kept as the second size selected sample, called XXL. The supernatant from this was used for the next cascade stage. This was repeated for 1000rpm (188g), 1500rpm (422g), 2500rpm (1174g) and 3500rpm (2300g), yielding samples: XL, M, S, XS. The cascade was stopped at 3500rpm due to low quantities of graphene remaining at higher centrifugation speeds.

A small portion of each dispersion was kept for TEM analysis and Raman spectroscopy with the rest being vacuum filtered to make films using 0.45μm pore size (47mm diameter) nylon membranes (Whatman) for samples containing large nanosheets. For the small nanosheet samples, 0.02 μm (47mm diameter) alumina membranes (Whatman) were used to make sure all nanosheets were being collected during the filtration. Also, for the samples prepared at higher rpm, there was not enough material to make free standing films (using the 47mm diameter membranes). Therefore, after the initial filtration, it was re-dispersed in a small volume (approx 30mL) of fresh NMP by bath sonication for 15 minutes. This was then filtered using a 0.02 μm, 13 mm pore diameter alumina membrane (whatman) to produce films thick enough to be free standing. All films were dried in vacuum oven at 100°C for 2 days.

Low-resolution bright field transmission electron microscopy (TEM) imaging was preformed using a JEOL 2100, operated at 200kV. Holey carbon grids (400mesh) were purchased from Agar Scientific and prepared by diluting a dispersion to a low concentration and drop casting onto a grid placed on a filter membrane to wick away excess solvent. Statistical analysis was performed to find the nanosheet dimensions by measuring the longest axis of the nanosheet and assigning it as "length", L, with the width, $w=L/k$, defined as the dimension perpendicular to L. SEM images were obtained using a ZEISS Ultra Plus (Carl Zeiss Group), 2 kV accelerating voltage, 30 μm aperture, and a working distance of approximately 1-2 mm. The samples were loaded onto the SEM stub using sticky carbon tape.

Samples were prepared for Raman spectroscopy by vacuum filtering a small quantity (2-5mL) of dispersion onto 0.02 μm, 13 mm pore diameter alumina membranes (whatman) to make films and these were dried in the same manner discussed above. Raman spectroscopy was performed on the graphene samples using a Horiba Jobin Yvon LabRAM HR800 with 532 nm excitation laser in air under ambient conditions. The Raman emission was collected by 100× objective lens (N.A. = 0.8, spot size ~1 μm). To avoid sample heating we carried out all Raman experiments at 10% of maximum laser power (<2 mW). A mapping over a 20×20 μm^2 sample

area was performed in each case in 2 μm steps. The spectra displayed are the baseline-corrected average of 120 individual spectra.

Specific surface area and surface energy measurements were carried out on a Surface Energy Analyser (SEA) IGC (Surface Measurement Systems (SMS), UK). All IGC samples were packed into silanised glass columns of internal diameter (ID) of 2 mm and length 30 cm. Silanised glass wool was used to plug both ends of column containing to sample to prevent machine contamination. For specific surface area measurement 10-15 mg of sample were packed into a 2mm ID column and preconditioned at 150 $^{\circ}$C under helium with flow rate 20 mL/min to remove and surface moisture and residual solvent. The peak max method was used for the retention time. A series of increasing probe concentrations of octane at 20 $^{\circ}$C and flow rate 20 mL/min were injected into the column to get an adsorption isotherm. Methane was used to calculate the column dead time. From this, the BET equation was applied using the SMS Cirrus Plus software to get the samples specific surface area.

The surface energy of the samples was measured by packing columns with a mass that corresponds to a surface area of 0.5 m^2; this is known from specific surface area measurements. The samples were preconditioned in the same way as previously described. Alkane probes (octane, heptane, hexane) were used to measure the dispersive surface energy. Coverage values ranging from 0.0075 to 1 were used to measure surface energy profiles of the samples. The peak centre of mass (COM) method was used to measure retention time. Surface energy measurements were performed at 90 $^{\circ}$C. The Cirrus plus software was used for all calculations. Chromatogram elution times were measured using a flame ionising detector (FID). The accuracy of the reported γ_d values depends heavily on the quality of the linear fit of the alkane line since the Dorris-Gray surface energy value depends on the square of the slope as show in equation 5. As a result we only used values where R^2>0.99 for alkane line fits. The uncertainty in γ_d measurements is explored in more detail by Ylä-Mäihäniemi et al.(56)
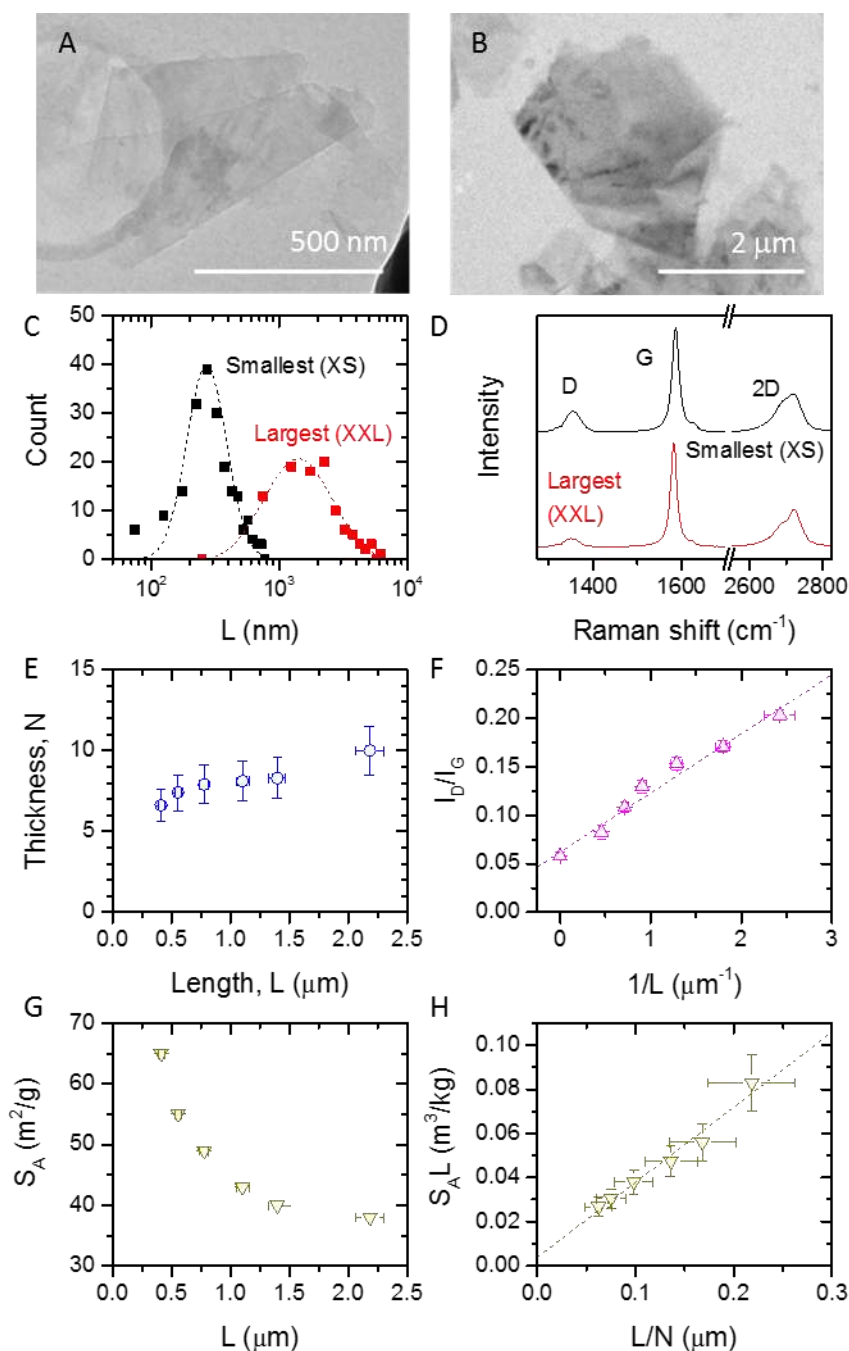
ACKNOWLEDGEMENTS:

Figures

Figure 1: Basic characterisation of liquid exfoliated graphene. A-B) Example TEM images of nanosheets from the smallest (A) and largest (B) fraction. C-D) Histograms showing length distributions (C) and Raman spectra (D) for the smallest and largest fractions. In C, the dashed lines are lognormal fits. E) Map showing nanosheet thickness (*i.e.* monolayers per nanosheet, measured from Raman 2D band) and length (measured by TEM) for the six fractions studied in this work. F) Raman D-band:G-band intensity ratio plotted versus inverse nanosheet length.

G) Specific nanosheet surface area plotted versus length. H) Linearized surface area plot. The line is a fit to equation 7b.
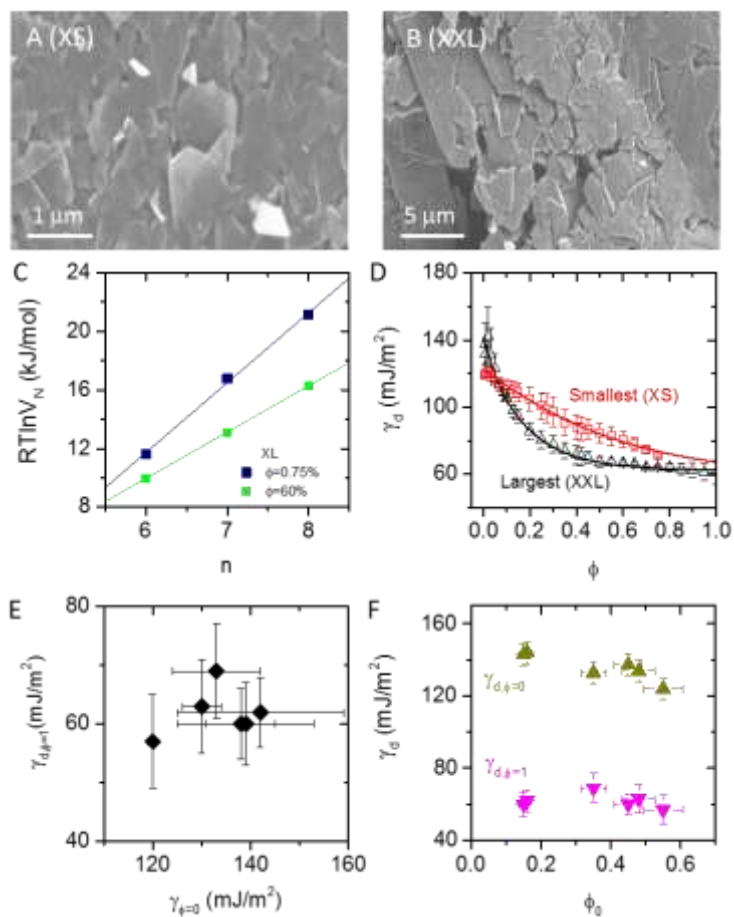

Figure 2: Inverse gas chromatography data. (A-B) SEM images of reaggregated solids used in the IGC measurements showing A) the smallest and B) the largest nanosheets. (C) The Gibbs free energy of adsorption ($RTlnV_N$) as a function of alkane number for two coverage values of the sample prepared by centrifuging at 300 and 500 rpm. The slope of the line is used for the calculation of γ_d using the Dorris-Gray formula (equation 5). (D) Dispersive surface energy, γ_d, measured as a function of surface coverage, ϕ, for the largest and smallest nanosheet fractions. As coverage increases, the surface energy decreases from its zero-coverage value, $\gamma_{d,\phi=0}$, toward its asymptotic value of $\gamma_{d,\phi=1}$. The solid lines are fits to equation 8b. (E) Fit values of $\gamma_{d,\phi=1}$ plotted against $\gamma_{d,\phi=0}$. This shows no correlation indicating that they are independent of each other. (F) $\gamma_{d,\phi=0}$ and $\gamma_{d,\phi=1}$ as a function of the decay constant (ϕ_0).
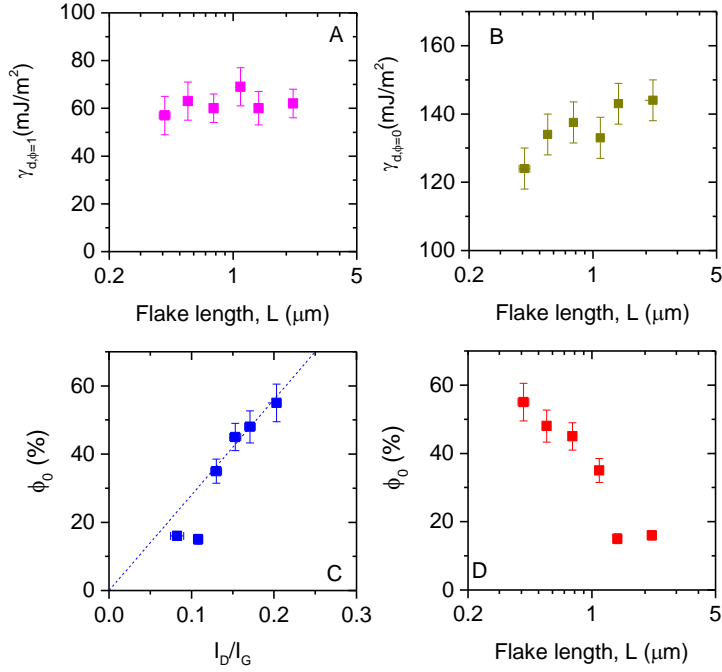
Figure 3: (A) Full-coverage surface energy, $\gamma_{d,\phi=1}$, plotted as a function of mean flake length (L) showing $\gamma_{d,\phi=1}$ to be size independent. (B) Zero-coverage surface energy, $\gamma_{d,\phi=0}$, plotted as a function of L. (C-D) Decay constant, ϕ_0, plotted as a function of C) I_D/I_G and D) L.
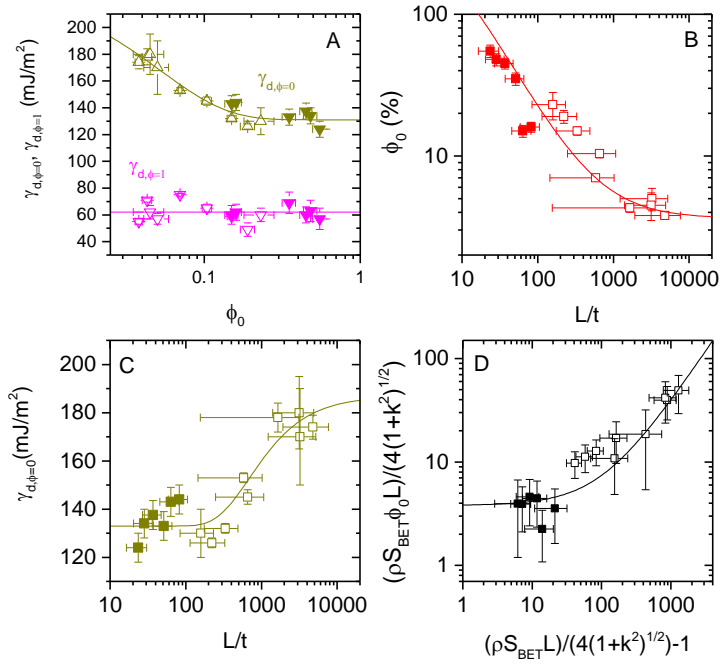

Figure 4: Comparison of surface energy data for both graphene (filled symbols) and graphite (open symbols). A) Zero- and full-coverage surface energies plotted as a function of decay

constant, ϕ_0. The dark yellow line is a fit to equation 11 while the magenta line represents the global mean of 62 mJ/m^2. B) Decay constant plotted against platelet length/thickness aspect ratio (L/t). The line is a fit to equation 9b. C) Zero-coverage surface energies plotted as a function of L/t. The line is a fit to equation 10. D) Data parameterised according to equation 12. The line is a linear fit.

References

1.   Novoselov KS, Fal'ko VI, Colombo L, Gellert PR, Schwab MG, Kim K. A roadmap for graphene. Nature. 2012;490(7419):192-200.
2.   Israelachvili J. Intermolecular and Surface Forces. Second Edition ed: Academic press; 1991.
3.   Lazar P, Karlicky F, Jurecka P, Kocman M, Otyepkova E, Safarova K, et al. Adsorption of Small Organic Molecules on Graphene. Journal of the American Chemical Society. 2013;135(16):6372-7.
4.   Ulbricht H, Zacharia R, Cindir N, Hertel T. Thermal desorption of gases and solvents from graphite and carbon nanotube surfaces. Carbon. 2006;44(14):2931-42.
5.   Wang W, Dai SY, Li XD, Yang JR, Srolovitz DJ, Zheng QS. Measurement of the cleavage energy of graphite. Nature Communications. 2015;6.
6.   Harvey A, He XY, Godwin IJ, Backes C, McAteer D, Berner NC, et al. Production of Ni(OH)(2) nanosheets by liquid phase exfoliation: from optical properties to electrochemical applications. Journal of Materials Chemistry A. 2016;4(28):11046-59.
7.   Fowkes FM. Attractive forces at interfaces. Industrial & Engineering Chemistry. 1964;56:40-52.
8.   Hernandez Y, Nicolosi V, Lotya M, Blighe FM, Sun Z, De S, et al. High-yield production of graphene by liquid-phase exfoliation of graphite. Nature nanotechnology. 2008;3(9):563-8.
9.   Ferguson A, Caffrey IT, Backes C, Coleman JN, Bergin SD. Differentiating Defect and Basal Plane Contributions to the Surface Energy of Graphite Using Inverse Gas Chromatography. Chemistry of Materials. 2016;28(17):6355-66.
10.   Dai J-F, Wang G-J, Wu C-K. Investigation of the Surface Properties of Graphene Oxide and Graphene by Inverse Gas Chromatography. Chromatographia. 2014;77:299-307.
11.   Dai J, Wang G, Ma L, Wu C. Study on the surface energies and dispersibility of graphene oxide and its derivatives. Journal of Materials Science. 2015;50:3895-907.
12.   Wang S, Zhang Y, Abidi N, Cabrales L. Wettability and Surface Free Energy of Graphene Films. Langmuir. 2009;25(18):11078-81.
13.   Shin YJ, Wang Y, Huang H, Kalon G, Wee ATS, Shen Z, et al. Surface-energy engineering of graphene. Langmuir. 2010;26:3798-802.
14.   Kozbial A, Li Z, Conaway C, McGinley R, Dhingra S, Vahdat V, et al. Study on the surface energy of graphene by contact angle measurements. Langmuir. 2014;30:8598-606.
15.   Li Z, Wang Y, Kozbial A, Shenoy G, Zhou F, McGinley R, et al. Effect of airborne contaminants on the wettability of supported graphene and graphite. Nature Materials. 2013;12:925-31.
16.   Wu CK, Wang GJ, Dai JF. Controlled functionalization of graphene oxide through surface modification with acetone. Journal of Materials Science. 2013;48:3436-42.
17.   Raj R, Maroo SC, Wang EN. Wettability of graphene. Nano Letters. 2013;13:1509-15.
18.   Annamalai M, Gopinadhan K, Han Sa, Saha S, Park H-J, Cho EB, et al. Surface energy and wettability of van der Waals structures. Nanoscale. 2016.
19.   Lazar P, Otyepkova E, Banas P, Fargasova A, Safarova K, Lapcik L, et al. The nature of high surface energy sites in graphene and graphite. Carbon. 2014;73:448-53.
20.   Grimsey IM, Feeley JC, York P. Analysis of the surface energy of pharmaceutical powders by inverse gas chromatography. Journal of Pharmaceutical Sciences. 2002;91:571-83.

21.   Zeki Y. Al-Saigh PM. Study of polymer-polymer interaction coefficients in polymer blends using inverse gas chromatography. Macromolecules. 1984;17(4):803-9.

22.   Ali SSM, Heng JYY, Nikolaev AA, Waters KE. Introducing inverse gas chromatography as a method of determining the surface heterogeneity of minerals for flotation. Powder Technology. 2013;249:373-7.

23.   Mukhopadhyay P, Schreiber HP. Aspects of acid-base interactions and use in IGC. Colloids and Surfaces A: Physicochemical and Engineering Aspects. 1995;100:47-71.

24.   Mohammadi-Jam S, Waters KE. Inverse gas chromatography applications: A review. Advances in Colloid and Interface Science. 2014;212:21-44.

25.   Adam Voelkel KB, Katarzyna Adamska, Beata Strzemiecka. Determination of Hansen Solubility Parameters by Means of Gas-Solid Inverse Gas Chromatography. Adsorption Science & Technology. 2008;26(1-2):93-102.

26.   Tyagi OS, Deshpande DD. Inverse gas chromatography of poly(n-butyl methacrylate): Effect of flow rate on specific retention volume and detection of glass transition temperature. Journal of Applied Polymer Science. 1987;34:2377-88.

27.   James AT, Martin AJP. Gas-liquid partition chromatography; the separation and micro-estimation of volatile fatty acids from formic acid to dodecanoic acid. The Biochemical journal. 1952;50:679-90.

28.   Ortmann F, Bechstedt F, Schmidt WG. Semiempirical van der Waals correction to the density functional description of solids and molecular structures. Physical Review B - Condensed Matter and Materials Physics. 2006;73:1-10.

29.   Carel J. Van Oss MKC, Robert J. Good. Interfacial Lifshitz-van der Waals and polar interactions in macroscopic systems. Chem Rev. 1988;88(6):927-41.

30.   Ferguson A, Khan U, Walsh M, Lee K-Y, Bismarck A, Shaffer MSP, et al. Understanding the dispersion and assembly of Bacterial Cellulose in Organic Solvents. Biomacromolecules. 2016;17:1845-53.

31.   Shi B, Wang Y, Jia L. Comparison of Dorris-Gray and Schultz methods for the calculation of surface dispersive free energy by inverse gas chromatography. Journal of chromatography A. 2011;1218:860-2.

32.   Dong S, Brendlé M, Donnet JB. Study of solid surface polarity by inverse gas chromatography at infinite dilution. Chromatographia. 1989;28:469-72.

33.   Papirer En, Li S, Balard H, Jagiello J. Surface energy and adsorption energy distribution measurements on some carbon blacks. Carbon. 1991;29:1135-43.

34.   Dorris GM, Gray DG. Adsorption of n-alkanes at zero surface coverage on cellulose paper and wood fibers. Journal of Colloid and Interface Science. 1980;77:353-62.

35.   Ho R, Wilson DA, Heng JYY. Crystal habits and the variation in surface energy heterogeneity. Crystal Growth and Design. 2009;9:4907-11.

36.   Huson MG, Church JS, Kafi AA, Woodhead AL, Khoo J, Kiran MSRN, et al. Heterogeneity of carbon fibre. Carbon. 2014;68:240-9.

37.   Kondor A, Quellet C, Dallos A. Surface characterization of standard cotton fibres and determination of adsorption isotherms of fragrances by IGC. Surface and Interface Analysis. 2015;47:1040-50.

38.   Paton KR, Varrla E, Backes C, Smith RJ, Khan U, O'Neill A, et al. Scalable production of large quantities of defect-free few-layer graphene by shear exfoliation in liquids. Nature Materials. 2014;13:624-30.

39.   Backes C, Szydłowska BM, Harvey A, Yuan S, Vega-Mayoral V, Davies BR, et al. Production of Highly Monolayer Enriched Dispersions of Liquid-Exfoliated Nanosheets by Liquid Cascade Centrifugation. ACS Nano. 2016:acsnano.5b07228.

40.   Backes C, Paton K, Hanlon D, Yuan S, Katsnelson M, Houston J, et al. Spectroscopic metrics allow in-situ measurement of mean size and thickness of liquid-exfoliated graphene nanosheets. Nanoscale. 2016.

41.   Ferrari AC, Meyer JC, Scardaci V, Casiraghi C, Lazzeri M, Mauri F, et al. Raman spectrum of graphene and graphene layers. Physical Review Letters. 2006;97:1-4.

42.   Eckmann A, Felten A, Mishchenko A, Britnell L, Krupke R, Novoselov KS, et al. Probing the nature of defects in graphene by Raman spectroscopy. Nano Letters. 2012;12:3925-30.

43.   Cancado LG, Jorio A, Ferreira EHM, Stavale F, Achete CA, Capaz RB, et al. Quantifying Defects in Graphene via Raman Spectroscopy at Different Excitation Energies. Nano Letters. 2011;11(8):3190-6.

44.   Gholamvand Z, McAteer D, Harvey A, Backes C, Coleman JN. Electrochemical Applications of 2-Dimensional Nanosheets: The Effect of Nanosheet Length and Thickness. Chemistry of Materials. 2016:acs.chemmater.6b00009.

45.   Cares-Pacheco MG, Calvet R, Vaca-Medina G, Rouilly a, Espitalier F. Inverse Gas Chromatography a tool to follow physicochemical modifications of pharmaceutical solids: crystal habit and particles size surface effects. International Journal of Pharmaceutics. 2015.

46.   Smith RR, Shah UV, Parambil JV, Burnett DJ, Thielmann F, Heng JYY. The Effect of Polymorphism on Surface Energetics of D-Mannitol Polymorphs. The AAPS Journal. 2016.

47.   Lazar P, Otyepková E, Karlický F, Čépe K, Otyepka M. The surface and structural properties of graphite fluoride. Carbon. 2015;94:804-9.

48.   Mohammadi-Jam S, Burnett DJ, Waters KE. Surface energy of minerals – Applications to flotation. Minerals Engineering. 2014;66-68:112-8.

49.   Wang S, Zhang Y, Abidi N, Cabrales L. Wettability and surface free energy of graphene films. Langmuir. 2009;25:11078-81.

50.   Hernandez Y, Lotya M, Rickard D, Bergin SD, Coleman JN. Measurement of Multicomponent Solubility Parameters for Graphene Facilitates Solvent Discovery. Langmuir. 2010;26(5):3208-13.

51.   Ho R, Naderi M, Heng JYY, Williams DR, Thielmann F, Bouza P, et al. Effect of milling on particle shape and surface energy heterogeneity of needle-Shaped crystals. Pharmaceutical Research. 2012;29:2806-16.

52.   Karlicky F, Otyepkova E, Banas P, Lazar P, Kocman M, Otyepka M. Interplay between Ethanol Adsorption to High-Energy Sites and Clustering on Graphene and Graphite Alters the Measured Isosteric Adsorption Enthalpies. Journal of Physical Chemistry C. 2015;119(35):20535-43.

53.   Krasheninnikov AV, Nieminen RM. Attractive interaction between transition-metal atom impurities and vacancies in graphene: a first-principles study. Theoretical Chemistry Accounts. 2011;129(3-5):625-30.

54.   Rafiee J, Mi X, Gullapalli H, Thomas AV, Yavari F, Shi YF, et al. Wetting transparency of graphene. Nature Materials. 2012;11(3):217-22.

55.   Lotya M, Hernandez Y, King PJ, Smith RJ, Nicolosi V, Karlsson LS, et al. Liquid phase production of graphene by exfoliation of graphite in surfactant/water solutions. Journal of the American Chemical Society. 2009;131:3611-20.

56.   Ylä-Mäihäniemi PP, Heng JYY, Thielmann F, Williams DR. Inverse gas chromatographic method for measuring the dispersive surface energy distribution for particulates. Langmuir : the ACS journal of surfaces and colloids. 2008;24:9551-7.